https://doi.org/10.5194/amt-2019-191
Preprint. Discussion started: 24 June 2019

Atmospheric Measurement Techniques Discussions
Open Access
EGU

On-flight intercomparison of three miniature aerosol absorption sensors using Unmanned Aerial Systems (UAS)

Michael Pikridas[1], Spiros Bezantakos[1], Grisa Močnik[2, 3], Christos Keleshis[1], Fred Brechtel[4], Iasonas Stavroulas[1,5], Gregoris Demetriades[1], Panayiota Antoniou[1], Panagiotis Vouterakos[1], Marios Argyrides[1], Eleni Liakakou[5], Luka Drinovec[2,3], Eleni Marinou[1,6], Vassilis Amiridis[5], Mihalis Vrekoussis[1,7,8], Nikolaos Mihalopoulos[1,5] and Jean Sciare[1]

[1]*Energy Environment and Water Research Center, The Cyprus Institute, Nicosia 1645, Cyprus*
[2]*Aerosol d.o.o., 1000 Ljubljana, Slovenia*
[3]*Jozef Stefan Institute, 1000 Ljubljana, Slovenia*
[4]*Brechtel Mfg. Inc., 1789 Addison Way, Hayward, CA 94544 U.S.A.*
[5]*Institute for Environmental Research and Sustainable Development, National Observatory of Athens, 15236, Athens, Greece*
[6]German Aerospace Center (DLR), Earth Observation Center, 82234 Weßling, Oberpfaffenhofen, Germany
[7]*Institute of Environmental Physics, U. of Bremen, Otto-Hahn-Allee 1, D-28359 Bremen, Germany*
[8]*Center of Marine Environmental Sciences - MARUM, D-28359 Bremen, Germany*

The present study investigates for the first time, the ground and flight performances of three miniaturized aerosol absorption sensors integrated on-board of Unmanned Aerial Systems (UAS). These sensors were evaluated during two contrasted field campaigns performed respectively at an urban site (Athens, Greece) impacted mainly by local traffic and domestic wood burning sources and at a remote regional background site (Agia Marina, Cyprus) impacted by long-range transported sources including dust.

The three sensors were intercompared at the ground level against two commercially available instruments (MAAP and AE33) used as a reference. The measured signal of the three sensors was converted into absorption coefficient, equivalent black carbon concentration (eBC) and, when applicable, to signal saturation corrections following the suggestions of the manufacturers. Despite the diversity of the aerosol origin, chemical composition, sources and concentration levels during the two campaigns, the aerosol absorption sensors exhibited similar behavior against the reference instruments. The deviation from the reference during both campaigns concerning (eBC) mass was less than 8%, suggesting that those miniature sensors that report BC mass are tuned/corrected to measure more accurately eBC rather than the absorption coefficient which deviated at least 15%.

The overall potential use of miniature aerosol absorption sensor on-board UAS is also illustrated here. UAS-based absorption measurements were used to investigate the vertical distribution of eBC over Athens up to 1 km above sea level during January 2016, reaching the top of the planetary boundary layer (PBL). Our results highlighted a heterogeneous boundary layer concentration of absorbing aerosol especially in the early morning hours with the concurrent peak traffic emissions at ground-level and fast development of the boundary layer. Vertical homogeneity was achieved when the boundary layer depth became stable.

https://doi.org/10.5194/amt-2019-191
Preprint. Discussion started: 24 June 2019

1. Introduction

Atmospheric aerosol particles scatter and absorb incoming solar radiation, thus directly affecting the radiative balance of the atmosphere (Haywood and Boucher, 2000). Their contribution to climate change is still associated with large uncertainties when estimating their radiative forcing (RF) (Bond et al., 2013; IPCC, 2013). A major contributor to these uncertainties is the RF induced by black carbon (BC), which among different numerical climate models exhibits a relative standard deviation exceeding 40% (Myhre et al., 2013), while in a more recent study it ranged from 0.14 to 1.19 (90% C.I) with an average value of 0.53 Wm^{-2} (Wang et al., 2016). Major factors responsible for the wide range of the BC's RF include the inaccurately predicted BC emission rates, the interaction of BC with clouds and its vertical distribution (Bond et al., 2013). In addition, BC has been identified to reduce the albedo of snow surfaces (Hadley and Kirchstetter, 2012) and suppress the turbulence of the boundary layer (Wilcox et al., 2016).

An array of techniques and instruments is employed worldwide for increasing the spatial/temporal resolution of BC observations to help reducing these uncertainties. The instrumentation employed uses different operating principles, including off-line or near-real-time on-line methods for measuring Elemental Carbon such as the thermal and gas-analytical method (EC; Birch and Cary, 1996; Zíková et al., 2016), as well as on-line, near real-time methods, which are mainly based on the aerosol light absorbing properties of BC (cf., Petzold et al., 2013, Moosmüller et al., 2009 and references therein for more details).

Most of the aerosol absorption observations available in the literature are usually conducted at ground level. Consequently, they miss critical information regarding the vertical distribution of aerosol absorption which is a critical parameter to constrain atmospheric models and accurately assess aerosol radiative forcing effects. One way to fill this gap is by conducting manned airborne aerial absorption measurements (Kassianov et al., 2018; Katich et al., 2018; Sedlacek et al., 2018). However, these are costly and cover a limited time period. The use of small scale-miniaturized sensors on-board of small unmanned aerial systems (UAS) or tethered balloons could provide cost-effective alternatives able to fill this gap and to enhance the vertical and temporal density of aerosol absorption observations.

Aerosol absorption instrumentation operating on-board manned aircrafts has been qualified through many intercomparison studies; contrary, their miniaturized counterparts' behavior is yet poorly demonstrated. The measurement quality delivered by these sensors during flight is challenged by fast changes in pressure, temperature, and humidity; which are difficult to assess at ground level.

UAS is a viable option to obtain valuable information on aerosol absorption vertical distribution. In fact, the reduced size, weight, and power needs of these systems, along with the reduced cost of the platforms and instrumentation, make them suitable for these operations with huge potentials currently poorly demonstrated. In addition, they have the advantage of better controllability over balloons and zeppelins, since the latter are more delicate at stronger winds (Jensen et al., 2007, Inoue et al., 2000). Even though small UAS are subject to significant payload restrictions compared to manned aircrafts, they have a distinct advantage over their manned counterparts in terms of relatively low

https://doi.org/10.5194/amt-2019-191
Preprint. Discussion started: 24 June 2019

Atmospheric Measurement Techniques Discussions

platform cost, capability to perform autonomous flight operations and spatially dense data collection (due to low speed operation), to fly (closer to the ground) with greater spatial accuracy, and less workload (Villa et al., 2016). They have also the potential (yet not demonstrated) of the ground-based monitoring networks capabilities in providing long-term atmospheric observations.

In this work, we focus on vertical distribution of aerosol absorption performed during two intensive field studies at contrasted locations in the Eastern Mediterranean; an urban site (Athens, Greece) and a remote regional background site (Cyprus Atmospheric Observatory, CAO, Cyprus). The vertical distribution of aerosols in the Eastern Mediterranean is of particular importance because it lies at the crossroads of diverse air masses (Lelieveld et al., 2002), including mineral dust from Africa and the Middle East, pollution from Europe and nearby Middle East, and marine aerosol (Gerasopoulos et al., 2006; Erel et al., 2006, Kalivitis et al., 2007). The sites were selected to represent two different and contrasted sources of ambient aerosol, with high concentration levels of freshly emitted BC from traffic and/or biomass burning (domestic heating) in Athens and low concentration levels of aged regionally transported aerosol occasionally mixed with moderate levels of dust in Cyprus.

Aerosol vertical profiles were performed using several types of fixed and rotary wings unmanned aerial systems (UAS). In this work, three miniature attenuation monitors were characterized against ground based commercial instruments. Instead of characterizing their performances under controlled conditions, these monitors were tested and intercompared on-flight with different UASs and diverse absorbing aerosol concentrations and types.

2. Sampling Sites

Sampling was conducted at two contrasted locations in the Eastern Mediterranean basin; an urban site (Athens, Greece) for a 1-week intensive period starting from 14 January 2016 and a background location in Cyprus for a 1-month intensive campaign in April 2016.

2.1 Athens campaign

In the framework of the European project ACTRIS 2 (Aerosols, Clouds, and Trace Gases Research Infrastructure), three miniaturized absorption instruments were tested and intercompared for a period of one week (14-21 January 2016) onboard UAS over Athens, a city highly impacted by strong UV absorbing domestic heating biomass burning aerosols during winter (Florou et al., 2017; Fourtziou et al., 2017). Flights were conducted at Lofos Nymphon (37°58'19.68"N - 23°43'5.32"E) situated at the historical center of Athens, a metropolitan area of more than 4,000,000 inhabitants. Lofos Nymphon is a small rock plateau inside a small forested area (Fig. 1), at a 50 m elevation from its surroundings. Traffic roads, marked with red lines on Fig. 1, are located westerly of the site. The closest traffic road is 150 m away from the measuring site. In order to comply with air space restrictions made by the Hellenic civil aviation authorities at Lofos Nymphon, a multicopter, described in detail in Section 3.1.3, was selected for its capacity to take-off and land vertically.

https://doi.org/10.5194/amt-2019-191
Preprint. Discussion started: 24 June 2019

A total of 26 flights were performed during periods without precipitation or strong winds, lasted for 15min each reaching as high as 1 km above sea level (a.s.l.) altitude limit set by the Hellenic civil aviation authorities.

During this campaign, the flight strategy has been elaborated as the following: Two early morning flights were performed at an interval of c.a. one hour starting at sunrise (05:00 UTC) to investigate the stratification of the atmosphere (boundary layer, low free troposphere). Two late afternoon flights ending approximately at sunset (16:00 UTC) were performed to investigate the vertical mixing of urban emissions in the atmospheric column. On 19 January 2016, intensive (hourly) flights were performed to investigate the impact of the diurnal development of the boundary layer on the vertical distribution of absorbing aerosols. These flights are further discussed in Section 7.

Due to payload restrictions (2 kg maximum for scientific instrumentation), not all the miniature monitors could fly simultaneously. The monitors that could not fly were operated at the co-located National Observatory monitoring station at Lofos Nymphon, together with two commercially available instruments (Magee Scientific AE33 and Thermo MAAP). In addition, the absorption monitor on board the multi-copter has been measuring at ground level during 2-3 min before and after each flight for a direct comparison against ground-based instruments.

2.2 **Cyprus campaign**

In the framework of the European project BACCHUS (Impact of Biogenic versus Anthropogenic emissions on Clouds and Climate; towards a Holistic UnderStanding) a 1-month campaign (30 March - 28 April 2016) was performed at the Cyprus Atmospheric Observatory (CAO, 35° 2'17.97"N - 33° 3'28.50"E), a remote regional background site at the Agia Marina Xyliatou in Cyprus.

Vertical profiles of aerosol absorption were performed in a dedicated UAS airfield (35° 5'41.93"N - 33° 4'54.26"E) located at approximately 7 km north of the Cyprus Atmospheric Observatory (Fig. 1). The airfield, shown in Fig. 2, is associated with a 500 m radius (in x-y plane) UAS airspace and an additional 500 m radius buffer zone, yielding a total of 1 km radius flight zone granted by the Cypriot civil aviation authorities and extending up to a height of approximately 2.4 km a.g.l. (2.7 km a.s.l.).

The UAS flight strategy was designed at characterizing the boundary layer and free troposphere with respect to aerosol absorption, number size distribution, and ice nuclei (IN) concentrations. More information from the UAS-based IN measurements can be found in Schrod et al. (2017). UAS-based aerosol number size distribution are presented and discussed in Mamali et al. (2018). The typical UAS flight period usually spanned from sunrise (05:00 UTC) to 09:00 UTC. Two types of fixed wing UASs were used during this campaign; two skywalker UAS (Model X8) and one Cruiser UAS (see section 3.1). Skywalker X8 flights typically lasted 30 min, while each Cruiser flight lasted between 1-1.5 h. Vertical profiles were performed almost on a daily basis provided meteorological conditions were favorable, and engaged a team of eight persons (two pilots, two ground control station operators, two electronic/mechanical engineers and two scientific staff for the operation of the miniaturized instruments). In this work, only the absorption measurements will be examined corresponding to a total of 17 flights performed with Skywalker X8 and 6 flights with the Cruiser.

https://doi.org/10.5194/amt-2019-191
Preprint. Discussion started: 24 June 2019

Ground based absorption measurements were conducted at CAO using two commercially available instruments (Magee Scientific AE33 and Thermo MAAP, see section 3.2.2). CAO is located 6.74 km southerly and at a 200 m elevation higher of the airfield (Fig. 1). Because of no significant local contamination sources in the surrounding area (Kleanthous et al., 2014; Pikridas et al., 2018), it has been assumed that atmospheric composition at CAO and the UAS airfield were similar, allowing a direct comparison between ground and airborne measurements. During this campaign, regional dust transport originating from Africa was identified on two occasions, during 9^{th} and 20^{th} of April 2016 respectively (Schrod et al., 2017).

3. Instrumentation

3.1 Unmanned Aerial System Types

As mentioned above, three types of unmanned aerial systems (UAS) have been used in this study; they differ with respect to payload, autonomy, wing type and landing requirements. Their specifications and capabilities, described below, are summarized in Table 1. Despite having the ability to reach altitudes higher than 2 km a.g.l., the UASs were limited to 1 and 2 km during the Athens and CAO campaigns, respectively, due to restrictions posed by the civil aviation authorities.

3.1.1 UAS "Cruiser"

The Cruiser is a medium-size fixed-wing UAS (Table 1) with a payload capacity up to 12 kg which includes both the weight of the fuel to power the engine and the battery used for the instrumentation. The Cruiser's payload bay, the available space inside the UAS, measures 1.3×0.23×0.34 m (LxWxH) and it comes with a wingspan of 3.8 m. It has been configured with internal combustion two-stroke engine placed in a pusher configuration that can climb up to 3-4 km altitude with a maximum take-off weight of 35 kg. Depending on payload and environmental conditions the Cruiser can reach a flying endurance up to 8 hours. During flight, atmospheric sampling occurs at a velocity of 28±5 m s^{-1} which is the typical cruising air-speed of this type of UAS. Under its current configuration the environmental conditions to ensure a safe operation are limited to winds up to 13 m s^{-1} and temperatures below the dew point in order to prevent icing on the engine's carburettor. However, the engine can be upgraded with an electronic fuel injection system in order to fly under icing conditions and thus to higher altitudes. The Cruiser is equipped with an autopilot system (Micropilot MP2128G2) which includes all the sensors and telecommunication systems (e.g. GPS, barometric altimeter, accelerometer, air-speed sensor, electronic compass, modems, antennas) that allows autonomous flights with real-time monitoring and control from ground providing that predetermined flight plans are set. At any time the UAS operator is able to modify the active flight plan in real-time. In addition, the system is capable of detecting faults and alter its flight plan accordingly (e.g. automatically return to home upon communication loss). The modular design of the Cruiser facilitates switching instruments between scientific missions provided that the total mass does not exceed the payload limit. To support its multi-instrument capability, a central data acquisition system built around the National Instruments controller, myRIO with a variety of interface possibilities and a Graphical User Interface (GUI) has been developed. The NI graphical programming language of Labview has been utilized to develop the GUI

https://doi.org/10.5194/amt-2019-191
Preprint. Discussion started: 24 June 2019

Atmospheric Measurement Techniques Discussions

with capabilities of real-time visualization of the instrumentation data as well as controlling and automation of the on-board instruments. All the instruments and avionics sensitive to vibration shake have been mounted into the Cruiser fuselage using special anti-vibration dampers in order to isolate the high-frequency oscillations produced by the UAS engine. Vibration isolation is essential in order to improve the flying reliability of the UAS as well as to keep quality of the scientific measurements to its higher standards.
Due to the Cruiser's size, a flat (ideally paved) runway is required for take-off and landing. During the Cyprus campaign, the Cruiser was taking-off and landing on the CyI's private runway (see Fig. 2). Along with other aerosol instruments (Ice Nuclei sampler, Optical particle counter), the Cruiser UAS carried one miniature absorption instrument (AE51, see section 3.2.3).

3.1.2 UAS "Skywalker X8"

The Skywalker X8 is a small delta-wing type UAS with an electric motor providing the propulsion. Made by foam, it is a much smaller and lower cost UAS comparing to the Cruiser. Its wingspan is 2.10 m and its maximum take-off weight is about 5.5 kg. It can fly for approximately one hour up to 3 km altitude with a payload of c.a. 3 kg, which includes the battery (14.8V Lithium Polymer, 9Ah) that powers the motor. This UAS is equipped with the same avionics as the Cruiser. The Skywalker X8 can take-off using a bungee launcher catapult system and can land on its belly on any flat surface. The skywalker X8 UAS has been operating exclusively during the Cyprus campaign and carried only one miniature absorption instrument (DWP, see section 3.2.3).

3.1.3 UAS "Multicopter S1000+"

A modified version of the commercially available octocopter DJi S1000+ was used during the Athens campaign to overcome strong constraints related to a limited ground area to take-off and landing, and flying in the limited air space. This platform has been optimized to reach an altitude up to 1 km a.s.l. for a maximum take-off weight of 11 kg and a payload of 4 kg including the motor battery (22V Lithium Polymer, 22Ah). In order to ensure that sampling was not influenced by the turbulence created by the octocopter's blades, the sampling inlet was extended by 1 m out of the propeller flow. This distance ensured representative sampling during ascend. However, during descent, this length was not sufficient to avoid the created vortex if a columnar path was followed. During the Athens campaign, the landing site was near the edge of a cliff and inside an archaeological area where pedestrians could freely access, prohibiting deviation from a columnar flight path (Fig. 1). As a result the quality of the descent flights was compromised at the expense of safety and only ascending flights are used in this work.

3.2 Aerosol absorption instrumentation

3.2.1 Principle of operation

Aerosol absorbing component can be apportioned in real-time using optical methods. The most widely used method, utilizes an aerosol sample-laden filter area where light is transmitted through. Additionally, light is simultaneously transmitted via

https://doi.org/10.5194/amt-2019-191
Preprint. Discussion started: 24 June 2019

an aerosol-free (unloaded) filter spot (reference signal) and the attenuation is calculated based on Eq. 1.

$$ATN(\lambda) = 100 \times \ln\left(\frac{I_{ref}(\lambda)}{I_{sample}(\lambda)}\right) \qquad \textbf{\textit{Eq}. 1}$$

where $I_{ref}(\lambda)$ and $I_{sample}(\lambda)$ are the reference and sample light signals, respectively, and $ATN(\lambda)$ the attenuation at wavelength λ. The attenuation rate dATN(λ)/dt determines the attenuation coefficient ($b_{atn}(\lambda)$) based on Eq. 2.

$$b_{atn}(\lambda) = \frac{A \cdot dATN(\lambda)}{100Q \cdot dt} \qquad \textbf{Eq. 2}$$

where A is the sample spot area, Q the air flow rate and dt the time period the attenuation change is considered, which typically equals to 1s for all the miniaturized instruments examined in this study. The instrument specific $b_{atn}(\lambda)$ can be converted to absorption coefficient $b_{abs}(\lambda)$, when accounting for the multiple scattering effect caused by the filter and/or by the sampled particles, together with the filter loading effects that the latter are causing. Due to lack of a reference method for providing the aerosol absorption coefficient and because every manufacturer is using different filter materials, several empirical corrections have been proposed in the literature (e.g., Weingarter at al., 2003; Virkulla et al., 2005; Collaud Coen et al., 2010; Ogren, 2010, Drinovec et al., 2015). For instance, many studies reporting aethalometer measurements have been calculating $b_{abs}(\lambda)$ based on Eq. 3 (Weingarter at al., 2003):

$$b_{abs}(\lambda) = \frac{b_{atn}(\lambda)}{C \cdot R(ATN(\lambda))} \qquad \textbf{Eq. 3}$$

where C is the optical enhancement factor due to multiple scattering within the filter medium and $R(ATN(\lambda))$ describes any other effects caused by the particles loaded on the filter.

The equivalent black carbon (eBC) mass concentration (expressed in μg m^{-3}) can be calculated solely based on 880 nm wavelength $b_{atn}(\lambda)$ (Ramachandran and Rajesh, 2007), using either Eq. 4 or 5,

$$eBC = \frac{b_{atn}(880nm)}{\sigma_{atn}(880nm)} \qquad \textbf{Eq. 4}$$

$$eBC = \frac{b_{abs}(880nm)}{MAC(880nm)} \qquad \textbf{Eq. 5}$$

where $\sigma_{atn}(\lambda)$ is the mass attenuation cross section and MAC the mass absorption coefficient. Table 2 summarizes C and $\sigma_{atn}(\lambda)$ factors used for each instrument in this study.

Factor C is considered to be constant during each campaign as it is, relevant to the filter tape only, while R is unity for an unloaded filter and reduces when particles are deposited onto the filter (Weingarter at al., 2003). Other absorption monitor manufacturers are using different approaches for deriving $b_{abs}(\lambda)$, which can be found in sections 3.2.2 and 3.2.3 for the instruments used in this study. The filter strip of the miniaturized instruments evaluated in this study, is changed manually before every flight so to keep the attenuation during the mission below a threshold value of 10-20% for which loading correction is not required (Weingartner et al., 2003; Ferrero et al., 2011).

3.2.2 Ground-based (reference) instruments (AE33, MAAP)

To overcome the filter loading effect discussed previously, Drinovec et al. (2015) developed the "dual spot" aethalometer (Magee Scientific, model AE33), which uses two sample spots where particles are deposited with different flow rates and one 'blank' spot as reference. The principle idea behind this approach is that any artifact induced by the accumulation of the particles onto the filter will have the same characteristics (i.e., both sample spots are probing the same particles) but the magnitude of saturation on each spot will differ. By combining the results from both sample spots the measurements are extrapolated to zero loading and the compensated/corrected eBC mass and light absorption can be obtained without using any assumptions on the physicochemical properties of the measured particles.

Another approach for reducing the measuring biases in particle absorption coefficient induced by the accumulation of particles collected on the filter sample spot is employed by the Multiangle Absorption Photometer (MAAP) instrument (Thermo Fisher Scientific), which measures absorption of the collected particles and corrects it based on their scattering at different angles (Petzold and Schönlinner, 2004).

In this study, these two commercially available absorption monitors (Magee Scientific - Model AE33; Thermo Scientific Fisher - Multi Angle Absorption Photometer Model 5012) were used as a ground-based reference for UAS-based absorption measurements. Nominally MAAP measurements, which have been shown to agree well against reference methods (Sheridan et al., 2005), were used after being corrected based on Eq. 6 (Muller et al., 2011).

$$b_{abs}(637) = 1.05 MAC_{BC}^{MAAP} \cdot eBC \qquad \textbf{Eq. 6}$$

where $b_{abs}(637)$ is the absorption coefficient at 637 nm (expressed in Mm^{-1}), MAC_{BC}^{MAAP} the specific mass absorption coefficient of black carbon proposed by the MAAP manufacturer equal to 6.6 m^2 g^{-1} (Petzold and Schönlinner, 2004)and *eBC* the equivalent mass concentration of black carbon reported by the instrument (in μg m^{-3}). Equation 6 assumes that the nominal wavelength MAAP operates not at 670 nm, as proposed by the manufacturer, but at 637 nm as measured by Muller et al. (2011).
The absorption coefficient at wavelengths different than 637nm was calculated based on the Angstrom law (Eq. 7).

$$\tau(\lambda) = \tau(\lambda_0)\left(\frac{\lambda}{\lambda_0}\right)^{-\alpha} \qquad \textbf{Eq. 7}$$

where $\tau(\lambda)$ and $\tau(\lambda_0)$ are the calculated and reference absorption parameters and α the angstrom exponent. For the MAAP instrument, the reference absorption (λ_0) is the one based on Eq. 6 at 637nm. The angstrom exponent was calculated by linear regression of the natural logarithm of the seven wavelength absorption coefficients measured by AE33 (370, 470, 520, 590, 660, 880 and 950 nm) and used for extrapolating into shorter and longer wavelengths of the absorption coefficients measured by the MAAP. The reported *eBC* measurements of AE33 were used to

https://doi.org/10.5194/amt-2019-191
Preprint. Discussion started: 24 June 2019

calculate $b_{atn}(\lambda)$ and $b_{abs}(\lambda)$ based on Eq. 3 and 4 and using values of mass attenuation cross section and optical enhancement factor reported in the literature (Table 2). Loading correction was not applied to the AE33 measurements as it incorporates a loading compensation scheme (Drinovec et al., 2015).

The AE33 was always operated at a 1 min time resolution; the MAAP operated at a 30 min time resolution during the Athens campaign and at a higher (2 min) time resolution during the CAO campaign.

During both campaigns lidar measurements at 532 nm from the EARLINET PollyXT-NOA system, described by Engelmann et al., 2016, was used to detect the PBL depth. During the Athens campaign, measurements were collocated with the in-situ measurements described above. During the Cyprus campaign, the PollyXT measurements were located 21 km east of the ground based measurements. Nevertheless, spatiotemporal homogeneity has been observed between the two sites for that specific period (Mamali et al., 2018; Marinou et al., 2018). The PollyXT lidar quicklooks from both campaigns can be found online (http://polly.tropos.de).

3.2.3 Miniature Absorption Monitors (AE51, DWP, STAP)

Three miniaturized instruments having optimal specifications to fly onboard UAS were evaluated. They consist of 1) a single wavelength commercially available absorption monitor (Aethlabs, Model AE51), 2) a Dual Wavelength Prototype (DWP) monitor based on AE51 model concept and 3) a Tricolor Absorption Photometer (Brechtel Inc - Model 9406). These 3 instruments will be referred in the following as AE51, DWP and STAP respectively. Table 3 summarizes the characteristics of each monitor.

The AE51 is the lightest instrument (150 g) which is a major asset for UAS observations. On the other hand, and due to a relatively low air sampling flow rate (0.1-0.2 L min^{-1} set by the user), it may lack sensitivity for low concentrations of absorbing material which can be an issue when investigating the low amounts of aerosols usually met in the free troposphere. The two other instruments (DWP and STAP) have a higher flow rate (2 and 1.3 L min^{-1}, respectively) which may improve sensitivity for low concentrations. These two instruments have also the potential to derive additional information regarding absorbing material other than black carbon using the Aethalometer model reported by Sandradewi et al. (2008). On the other hand, they are significantly heavier (660 g and 1.1 kg for STAP and DWP, respectively) which may represent a major constrain for UAS flights.

The STAP (Single channel Tri-color Absorption Photometer, Brechtel Model 9406), formerly named ABS (see Bates et al., 2013) has been manufactured following the design of the Particle Soot Absorption Photometer (PSAP; Bond et al., 1999), except that the detection electronics has been completely redesigned to significantly improve signal-to-noise and provide a detection limit of ~0.2 Mm^{-1}. Light from three LED sources with wavelengths centered at 445, 515 and 633 nm (Table 3) is alternatively transmitted through glass windows with 50 Hz frequency. The diffused light, which is transmitted through two filter-holding spots that typically carry glass fiber filters, is continuously monitored by two photodetectors. One filter spot is only loaded with the sample aerosol while the other remains sample-free, acting as a reference. The highest sampling rate achieved is 1 Hz. The glass fiber filters minimize light from being transmitted in the forward direction (forward scattering) thus reducing the bias due to scattering by the collected aerosol, while they allow the sampled particles to be

https://doi.org/10.5194/amt-2019-191
Preprint. Discussion started: 24 June 2019

embedded within the filter, integrating them in the optically diffusive environment. A laminar flow element is used to measure the sample volumetric flow rate in real time and an on-board software automatically controls the small integrated vacuum pump to maintain a constant sample volume flow independent of UAV altitude. The sample flow is dried to eliminate artifacts due to water uptake by the filters.

Calculated absorption from the 3 miniature instruments was derived directly from the sample and reference signals, using Eq 1, 2 and 3 without taking into account the computed eBC or $b_{atn}(\lambda)$ reported by the instruments. For AE51 and DWP the difference between the calculated and reported absorption values was 0.01% or less. The $b_{atn}(\lambda)$ reported by STAP was initially processed with a 60 s moving average which was deemed too long. To address that issue, a custom-made moving average was applied to the raw (1Hz time resolution) $b_{abs}(\lambda)$ signal in order to reduce the signal-to-noise ratio (more details in Section 4). Furthermore, this custom moving average allowed a more accurate determination of $b_{abs}(370)$ and $b_{abs}(880)$ based on Eq. 7 for STAP. The STAP manufacturer suggests conversion from $b_{atn}(\lambda)$ to $b_{abs}(\lambda)$ based on Eq. 8 (Ogren et al., 2010), which also accounts for loading artifacts. This conversion has been applied only on STAP measurements instead of Eq. 3.

$$b_{abs}(\lambda) = \frac{0.85 b_{atn}(\lambda)}{1.22(1.0796\frac{\mathrm{I}(t)}{I_{wf}} + 0.71)} \qquad \text{Eq. 8}$$

where $I(t)$ is the attenuation at given time and I_{wf} the measured attenuation under particle free air after changing the filter medium.

4. Data exploitation: Improvement of the Optimized Noise-reduction Averaging (ONA) Smoothing Algorithm

The three miniature absorption monitors were set to sample at a rate of 1 Hz. However, all measurements were subjected to non-negligible instrumental noise (defined as one single standard deviation of the absorption coefficient) making the data exploitation for short time intervals challenging. The use of a standard averaging method (average, rolling average, least squares fit) would require setting a fixed time step upon which all measurements will be averaged regardless of the signal-to-noise ratio. This will result to reduced noise but may compromise the need for high time (spatial) resolution as it is the case for UAS-based measurements. Instead, Hagler et al., (2011) proposed a method where the averaging step is not defined by the time, but is based on the measured attenuation. In that method, named Optimized Noise-reduction Averaging (ONA), $dATN(\lambda)/dt$ should only be positive or zero (but not negative). As a result, for a predefined configuration (sample volume, sample spot area), the same averaging attenuation step (ΔATN) will require more data points to be averaged during periods with low atmospheric concentrations (i.e lower time resolution) compared to periods with high atmospheric concentrations. Therefore, using ONA, the averaging time step is dynamically set to be inversely proportional to the sampled concentration (see also Eq. 2). Since the method is based on attenuation changes, it can only be applied to individual spots, where the sample is accumulated, in a continuous monitor or an individual filter in semi-continuous monitors such as the miniature absorption monitors investigated in this work.

https://doi.org/10.5194/amt-2019-191
Preprint. Discussion started: 24 June 2019

The algorithm proposed by Hagler et al. (2011) results in an integrated-like (fragmented) data structure which significant lowers the vertical resolution of our UAS-based absorption measurements (blue dots in Fig. 3). Additionally the algorithm assumes that the same attenuation step will be used for each wavelength independently of the fact that attenuation of shorter wavelengths usually progresses faster.

To cope with the above issues, an improvement of the ONA algorithm is proposed here. A moving average is implemented instead of the one applied in the ONA algorithm, resulting in a more continuous-like data structure and improved vertical resolution (red dots in Fig. 3). If more than one wavelength is monitored, then the improved ONA algorithm is applied to all wavelengths but based on the attenuation of the larger one, so to produce comparable averaging results.

The flow diagram of the proposed improved ONA algorithm is presented in Suppl. Fig. 1. A link to the actual code is also provided, via a file sharing portal, in the supplement. The user supplies attenuation, and instrument response (e.g. eBC mass, b_{abs}) as time series along with the desired attenuation step (ΔATN). If more than one wavelength is to be examined, they have to be specified. Initially, the longer wavelength is automatically selected and a time interval based on the desired ΔATN value is calculated for each data point. The calculated time interval includes attenuation values in the range [-0.5×ΔATN, + 0.5×ΔATN] centered at the selected data point. The time interval is limited to correspond to only one sample spot. The same averaging times are then applied to the remaining wavelengths, if any. Discrepancies could arise when abrupt concentration gradients are sampled e.g monitoring the vertical profile of a polluted boundary layer followed by clean air masses. In this case the rate of attenuation change will decrease, since the air mass contains less absorbing aerosol. If the concentration gradient between the two layers is large enough the algorithm may lead to fictitious shift of the boundary layer height because more data points from the clean air mass than the polluted boundary layer will be accounted for in the average. The discrepancy is solved if weights inversely proportional to the number of data points used for the average before (-0.5×ΔATN) and after (+ 0.5×ΔATN) the sample point to be examined are applied. The improved ONA algorithm incorporates filters that cope with this problem. Erroneous results may also arise from outliers in the time series, especially if small ΔATN are applied or if the time series are oversmoothed. An example of oversmoothing is shown in Fig.3 (green dots). For all the reasons discussed above, it is advised to examine the result using different ΔATN and against the raw input.

High ΔATN values will reduce noise but reduce the time (vertical) resolution. A ΔATN equal to 0.01, 0.03, 0.03 is suggested for AE51, DWP and STAP, respectively and these values take into account the air face velocity set for each instrument. Vertical profile case studies are therefore discussed later in Section 6 with the above proposed attenuation steps. Note that Hagler et al. (2011) suggests a higher ΔATN, equal to 0.05, for all monitors regardless of individual face velocity.

5. Quality Assurance

Despite that all the available methods have the scope of reporting the mass concentration of BC, discrepancies between the different techniques or even instruments that are based in the same operating principles have been reported (e.g.,

https://doi.org/10.5194/amt-2019-191
Preprint. Discussion started: 24 June 2019

Watson et al., 2005, Slowik et al., 2007, Müller et al., 2011). These discrepancies are not only attributed to the different measurement techniques/instruments used but also to the large variability of the physicochemical properties of atmospheric or laboratory generated carbonaceous particles. For instance, the optical properties of carbonaceous particles depend on their size and morphology (Bond and Bergstrom, 2006, Fernández et al., 2015), on their mixing state and/or coating thickness with other atmospheric relevant species, including sulfate, water, organic or dust (Lack et al., 2009, Lack and Cappa, 2010, Shiraiwa et al., 2010, Zhang et al., 2015, Liu et al., 2015). As a result, aerosol absorption measurements need to be associated with a comprehensive understanding of the methods and uncertainties associated with each instruments and how they have been operating in the field. Condensation or volatilization of water on the filter spot of the miniature sensors may greatly affects absorption measurements (Hale and Querry, 1972). In order to minimize this artifact, a custom-built (lightweight) silica-gel dryer was installed at the inlet of each miniature sensor and regenerated before each flight. It is noted that each sensor operated with its own inlet and dryer during both campaigns and even in when two sensors were airborne simultaneously in one UAS. However, to reduce weight, no size-selective inlet was employed. Ground based sensors were similarly configured; at least during UAS flights were ongoing.

5.1 Aerosol Absorption derived by AE33 and MAAP

During the Athens campaign AE33 and MAAP showed excellent agreement (R^2=0.98, N=381) with respect to the *eBC* mass concentration trend at a 30 min time resolution (Fig. 4). However, AE33 reported higher eBC by 20±11% compared to MAAP, and higher absorption coefficient at 370 and 880 nm of more than a factor 2. During the Cyprus campaign, the both monitors also showed very good agreement (R^2=0.89, N=1434) at a 30 min time resolution. However, similar to the Athens campaign, AE33 showed eBC mass concentration by 13±5% higher compared to MAAP, and higher absorption coefficient at 370 and 880 nm by almost a factor 2. Drinovec et al. (2015) suggested that AE33 could overestimate eBC up to approximately 7% when compared to MAAP. Muller et al. (2011) calculated the absorption coefficient at 637 nm of single spot aethalometers measuring ambient air and showed that it can be up to 60±20% overestimated when compared to MAAP. Finally, MAAP has been reported to underestimate eBC in polluted environments (Hyvärinen et al., 2013) when the measured eBC concentration exceeds 3 μg m^{-3}. Table 4 summarizes the results from both campaigns (illustrated in Fig 4). Clearly, this comparison suggests that AE33 and MAAP exhibit a better match with respect to eBC mass rather than with the absorption coefficient.

In the comparison presented above, MAAP was chosen as the reference instrument because it has been shown to exhibit good agreement against ambient absorption methods (Sheridan et al., 2005) that do not require correction schemes (e.g. photoacoustic spectrometers) and because its unit-to-unit variability reported to be small (approximately 5%; Muller et al., 2011). However, MAAP monitors absorption at a single wavelength and samples at lower temporal resolution than the one desired for this study (30 min in the Athens campaign and 2 min in the Cyprus campaign).

In the following sections, we investigate how measurements from miniature attenuation monitors relate to the commercial ones discussed in this section. AE33 is

https://doi.org/10.5194/amt-2019-191
Preprint. Discussion started: 24 June 2019

Atmospheric Measurement Techniques Discussions

always utilized as a reference because of its high temporal resolution (1 min). For this purpose, AE33 results are first scaled to match those of MAAP, to approximate, at least on average, the suggested "reference" values taking advantage the excellent trend agreement between these two instruments. The *eBC* by the AE33 was consequently decreased by 20% and 13%, $b_{abs}(370)$ was decreased by a factor of 2.4 and 1.93, and $b_{abs}(880)$ was decreased by a factor of 2.2 and 1.83 during the Athens and CAO campaigns, respectively.

5.2 UAS-based absorption measurements

The loading correction term in Eq. 3 was neglected in our study, assuming a value equal to unity when attenuation was low. It is noted that currently, most loading correction schemes are applied to continuous monitors that change sample spots automatically. Attenuation of AE51, provided by the instrument never exceeded 1% during the Athens campaign due to the combination of low sampling flow rate and limited sampling times (approximately 15 min) of each flight. During the Cyprus campaign it reached up to 2% because sampling time was higher (1-1.5 h) despite the lower measured *eBC* concentrations. Because of its higher sampling flow rate, the attenuation of DWP at 880 nm exceeded 15%, five times in each of the two campaigns. In order to examine whether measurements by DWP exceeding 10% attenuation were significantly affected by the filter loading effect, a comparison with respect to $b_{abs}(880)$ was conducted against both AE51 and AE33. The comparison results, shown in the supplementary material (Suppl Fig. 2), support the assumption of a loading correction (R) equal to unity was valid during both campaigns.

A second DWP monitor was installed in series behind the one which is been evaluated here in order to assess the possible impact of changes in Relative Humidity on the attenuation measurements. The second DWP was measuring signals downstream of the filter strip of the DWP; the hypothesis here is that both DWP should be similarly affected by artifacts induced by water absorption/desorption onto the filter strips. An underlying assumption is that both monitors were operating under the same temperature. Under normal (dry) conditions the second DWP should always report zero concentrations; this was the case during the Athens campaign with the exception of one flight performed on the 15th January 2016 when the silica gel dryer was removed. During this flight, the second DWP provided attenuation measurements deviating from zero, as high as 30 Mm^{-1} at 880 nm, suggesting that the first DWP measurements may also have been affected by sampling bias (Suppl. Fig. 3).

6. Comparison of miniature attenuation monitors against reference instruments

Since most the commercially available sensors provide BC readings (instead of absorption like STAP), we have decided to extend our absorption intercomparison to *e*BC. Despite BC being the most absorbing material in ambient air, others components, such as brown carbon and dust could also contribute especially at shorter wavelenghts (Andreae et al., 2006). In this work, the term *e*BC was chosen instead of BC (Petzold et al. 2013) to stress that BC in not the only absorbing material. In addition to *eBC*, aerosol absorption coefficients at 370 and 880 nm were also selected because two of the three miniaturized sensors measured at least at one of those wavelengths (see Table

https://doi.org/10.5194/amt-2019-191
Preprint. Discussion started: 24 June 2019

Atmospheric Measurement Techniques Discussions

3). Extrapolation based on angstrom law (Eq. 7) was applied for the monitors that did not measure at these two specific wavelengths.

6.1 Overview of the temporal and diurnal variability of eBC during the Athens and Cyprus campaigns

During the Athens campaign the average eBC concentration determined by AE33 was 1.5±2.1 μg m^{-3}, ranging from 0.3 to 15 μg m^{-3}. The presence of BC related to biomass burning (BC_{bb}), was identified and quantified throughout the campaign (Supp. Fig. 4), using the Sandradewi et al. (2008) model, but never exceeded 20% of the total eBC during daytime (05:00-15:00). During nighttime, BC_{bb} concentration was always elevated, reaching 40-60% of the total eBC that typically remained below 2 μg m^{-3}. On two occasions (14/01 16:00 – 15/01 05:00 and 21/01 15:00 –22/01 00:00) eBC exceeded 5 μg m^{-3} for several hours dominated by BC_{bb}. On average, BC_{bb} was identified from 16:00 UTC till 04:00 UTC of the following day and was enhanced by the low boundary layer observed during those hours and the need for heating due to low temperatures. Similar behavior attributed to biomass burning aerosol has been reported previously in Athens (Florou et al., 2017, Fourtziou et al., 2018) and other major Greek cities (Petrakakis et al., 2013; Pikridas et al., 2013). BC related to fossil fuel also exhibited a distinct diurnal pattern that included two maxima. The first was observed approximately 06:00 UTC that was attributed to the rush hour traffic period and the second during the night (after 16:00 UTC) simultaneously with the period when biomass burning related BC was observed. Increased biomass burning, especially during nighttime for domestic heating purposes, due to the economic crisis in Greece, has been reported for another major greek city (Saffari et al., 2013).

During the Cyprus campaign eBC measured by AE33 did not exceed 2 μg m^{-3} and most of the time it was found below 0.8 μg m^{-3}. The highest hourly concentration (1.9 μg m^{-3}) was observed on the 10th April 2016 (Supp. Fig. 5) when the site was influenced by air masses from N. Africa, and the lowest (<0.1 μg m^{-3}) on the 12 and 14th of April 2016. During the Cyprus campaign, dust transport from the Saharan desert was identified on 3 occasions (7-10, 15-17 and 21-27 April 2016) based on combined information from i) elevated coarse-mode particulate matter concentrations, ii) aerosol spectral properties of the entire atmospheric column measured by sun photometry and iii) back-trajectory analysis and iv) satellite pictures (MODIS AOD product). The diurnal pattern of eBC during the Cyprus campaign was relatively flat as expected in a remote background site, characterized by an almost invariable concentration approximately at 0.4 μg m^{-3} (campaign average equal to 0.39±0.24 μg m^{-3}).

6.2 Ground-based intercomparison of aerosol absorption

During the Athens campaign, each miniature sensor not performing vertical profiling, was operating at ground level in parallel with AE33 and MAAP, allowing a direct comparison. Additionally, the miniature sensors on board the multi-copter were measuring at ground level (2-3 min) before take-off and after landing. It is noted that the same setup (sampling lines, diffusion dryer) was utilized whether the miniature samples were mounted in the UAS platform or not. Based on the combination of these datasets resampled to 1 min (the time resolution of AE33), DWP exhibited good correlation, with respect to eBC against AE33 (R^2=0.90, slope=0.93, N=417) shown in

Fig. 5a, while the AE51 performed slightly poorer correlation (R^2=0.76, slope=0.94, N=125) (see Table 4). One possible explanation is the lower signal-to-noise ratio of AE51. Both monitors measured *eBC* concentrations lower by 6-7% compared to the reference measurements. STAP does not report eBC mass concentration and was excluded from this comparison for that purpose.

With respect to $b_{abs}(\lambda)$ at 370 and 880 nm, both STAP and DWP showed good correlation (R^2=0.89 and 0.87, N=519 and 417 for STAP and DWP, respectively) against AE33, while the correlation with AE51 was slightly poorer (R^2=0.76, N=125) at 880 nm (Fig. 5c).

However DWP overestimated $b_{abs}(880)$ by 29±20% compared to the corresponding reference measurements, even though the eBC mass, calculated from the same wavelength, was underestimated by 7%. Similar to DWP, AE51 overestimated $b_{abs}(880)$ by 30±12% even though eBC mass was underestimated by 6%. Both miniature sensors underestimate with respect to eBC but at the same time overestimate with respect to the absorption coefficient mainly due to the higher correction factor applied to the AE33 measurements concerning the latter (approximately a factor of 2) compared to the former (≈20%) to match those of MAAP as discussed in Section 5.1.

STAP was found to overestimate $b_{abs}(880)$ by 6±8.5% and underestimate $b_{abs}(370)$ by 7±7%. During a laboratory comparison (Muller et al., 2011) reported that a continuous single spot aethalometer (Magee Model AE31) overestimated b_{abs} compared to MAAP by 37-60% at 660 nm. The same study also reported underestimation of the absorption coefficient at 650 and 585 nm against MAAP of the Particle Soot Absorption Photometer (Radiance Research Model PSAP, the rack mounted equivalent of STAP) by 1-14%. These laboratory comparison results are similar to those reported in this study (AE51 overestimates and STAP underestimates by similar extent against the reference).

These results suggest that the miniature sensors intercompared during the Athens campaign, exhibit better agreement with respect to the parameter they report. Concerning AE51 and DWP this parameter was *eBC* concentration, which was within 10%, rather than the absorption coefficient, suggesting that the absorption coefficient should be preferentially calculated based on MAC values (Eq. 5) instead, if these are known or can be calculated. On the other hand, STAP that does not report eBC but b_{abs} exhibited good agreement, within 10%, against the reference on that property. The discrepancies discussed above lead to an average underestimation in the calculated angstrom exponent of DWP and STAP against that of AE33 by 13% and 12% respectively.

During the Cyprus campaign, aerosol absorption was also monitored at the ground by an AE33 and a MAAP located at CAO, approximately 7 km away and at 200 m higher elevation from the UAS airfield. Only DWP and AE51 were used during this campaign. Assuming homogeneity between the two sites, a direct comparison was conducted between ground and UAS measurements.

The comparison results, shown in Fig. 6, indicate that the correlation between the ground measurements and UAS (AE51 and DWP) measurements led to less satisfactory results compared to the Athens campaign (see also Table 4). The correlation between AE33 and DWP was still acceptable (R^2=0.71; N=91) with respect to *eBC* and the absorption coefficient at 370 and 880 nm at 1 min time resolution. But correlation

https://doi.org/10.5194/amt-2019-191
Preprint. Discussion started: 24 June 2019

between AE33 and AE51 was found as poor (R^2=0.32, N=48) with respect to *eBC* and $b_{abs}(880)$.

Atmospheric concentration of absorbing material (with respect to eBC) was found on average 4 times lower in Cyprus (mean of 0.39±0.24 μg m^{-3}) compared to Athens (mean of 1.5±2.1 μg m^{-3}), limiting the performance of the miniature sensors. Additionally, the range of atmospheric concentrations was also reduced by a factor of 6 in Cyprus (maximum hourly averaged eBC was 1.9 μg m^{-3}) compared to Athens (maximum hourly averaged eBC was 12.2 μg m^{-3}), leading to less favorable conditions for direct instrument-by-instrument comparisons. These conditions had a direct impact in the uncertainty related to the measurement agreement between the AE33 and the miniature monitors. During the Cyprus campaign, the uncertainty was always greater than the respective of the Athens campaign. As an example during the Cyprus campaign, DWP underestimated *eBC* by 6±20% and overestimated $b_{abs}(880)$ by 20±26%, while during the Athens one the respective numbers were 7±15% and 29±20% (Table 4). The effect was greater concerning AE51, which overestimated *eBC* by 22±52% and $b_{abs}(880)$ by 55±66%, while during the Athens campaign the respective numbers were 6±9% and 30±12% (Table 4). It is unclear whether the absorbing properties of the sampled aerosol (fresh at Athens and aged at Cyprus) had any effect on this comparison.

6.3 On flight intercomparison of aerosol absorption

During flights, vibrations as well as strong gradients of pressure, temperature, and RH may affect the performance of the miniature sensors. Due to extra weight issues, STAP and DWP could not fly simultaneously. However, the lower weight of AE51 enabled on-flight cross comparison with DWP and STAP, respectively during 8 flights of the Athens campaign. The correlation of AE51 airborne with both DWP and STAP was very good (R^2=0.65, N=493 and R^2=0.87, N=1875, respectively) provided that the sampled air was dried (Fig. 7) and the dataset conditioned as suggested in Section 4. Note that, if no smoothing is applied then the agreement deteriorates sharply (R^2=0.01) for either DWP or STAP. The ΔATN used for this comparison were 0.01, 0.03, and 0.03 for AE51, DWP, and STAP, respectively as suggested in Section 4. STAP is shown to underestimate b_{abs} by 12% compared to AE51 (Fig. 7), consistent with the comparison against AE33 discussed in Section 6.2. The very good correlation (comparison slope = 0.87) between the two when airborne also suggests that on average, no significant bias during the flights was present.

7. Diurnal Vertical Profiles of Black Carbon above Athens: A case study

As part of the Athens campaign, intensive vertical absorption profiles were performed with the objective to assess the influence of the diurnal development of the planetary boundary layer (PBL) on the vertical dispersion of ground-based black carbon emissions. UAS-based measurements were conducted for that purpose on the 19th of January at sunrise (05:38 UTC) and were continued on an hourly basis till the PBL depth exceeded the maximum height allowed to operate (1 km a.s.l.) approximately at 10:00 UTC. Two additional flights were conducted later in that day; one hour before and during sunset (15:38 UTC). The reconstructed vertical distribution of eBC based on the six ascending vertical profiles from 05:30 till 09:45 (UTC) is shown in Fig. 8, complemented by ground measurements during the same day by AE33. The actual vertical profiles for the entire day (N=8) are also shown in Fig. 9. To the best of our knowledge, this is the first time that the vertical dispersion of ground-based black carbon emissions is dynamically assessed above a city. Our results suggest a non-homogeneous boundary layer that evolved at a rate of 132 m h^{-1} during 19th January 2016 starting from an elevation of 265 m a.s.l. before sunrise. On the ground, *eBC* from the miniature monitor followed the diurnal pattern also observed on the ground by the reference instrument. At this low elevation and since 05:00 UTC *eBC* increased by a factor of 8, maximizing at 07:00 UTC. The emission's pattern and the angstrom exponent, calculated based on AE33 measurements, which was equal to 1.1 when concentrations maximized, suggest that this increase was due to local traffic emissions (see also Fig. 8). After 10:00 UTC *eBC* remained relatively stable at 1.5 μg m^{-3} (≈5 Mm^{-1} at 880 nm).

Above the PBL, which was determined by Polly-XT measurements (Baars et al., 2008; dashed red lines in Fig. 9), the measured concentration of eBC was always lower than the respective one measured within, by at least 20%. The highest eBC concentrations above the PBL were observed during sunrise and sunset (first and last diurnal profile in Fig. 9) equal to 1.9 and 2.0 μg m^{-3}, respectively. The lowest *eBC* concentration in this layer, equal to 0.3 μg m^{-3}, was observed at 06:30 UTC but steadily increased to 0.4, 0.9 and 1.7 μg m^{-3}during 07:38, 08:39 and 09:44 UTC, respectively. Due to flight restrictions, free tropospheric measurements could not be monitored after 10:00 UTC. PBL was also identified by vertical profiles of potential temperature which are in good agreement with those derived by Polly-XT

Before sunrise, our results suggest the presence of stable boundary layer in contact with the ground that has been radiatively cooled, and on top a residual layer. As the sun rises, the stable boundary layer's depth increases and simultaneously the residual layer is mixed with the free troposphere. During the 19th January 2016, mixing took place between 05:45-06:30 UTC. The concentration of eBC in the residual layer drops to near zero because the trapped pollutants are now diluted in the free troposphere.

However, the concentration of eBC above the boundary layer exhibited an increasing trend suggesting either convection of pollutants from the PBL or advections of regionally transported PM involving absorbing material that did not intrude the PBL. During the period when absorbing material was directly emitted from the ground and the boundary layer height increased (from 05:30-08:30 UTC), *eBC* dispersion inside the PBL was not homogeneous but was gradually decreasing with increasing altitude. The effect is more evident when emissions from the ground exhibited an increasing trend (approximately from 06:30-07:40 UTC). Once ground emissions reached their minimum and the PBL stabilized, the concentration inside the PBL became homogeneous (from 10:00 UTC till sunset). During sunset, stratification of a new stable boundary layer was observed and on top of it a new residual layer forming.

The vertical absorption distribution was reconstructed based on the absorption profiles shown in Fig.8, during 19 January 2016 between 05:34 and 09:36 (UTC) and also shown in Fig. 9 against PollyXT's range corrected signal.

8. Conclusions

Two field campaigns were conducted in Athens (Greece) and in CAO (Cyprus) in order to i) study the vertical distribution of aerosol absorption and ii) to evaluate the performance of three miniature absorption sensors in contrasted atmospheric environments against ground based reference instruments (MAAP and AE33). Measurements were conducted on the ground and air using three different models of UASs.

UAS-based aerosol sampling was dried to minimize the influence of water absorption/desorption on the filter strips and attenuation measurements. The influence of water on attenuation measurements was confirmed during the Athens campaign, by placing two DWP in series, with the second measuring filtered air from the exhaust of the first.

During January 2016, the miniature sensors sampled urban aerosols at the center of Athens, Greece. On the ground, STAP and DWP followed well the observed variations in absorbance ($R^2 \approx 0.90$) against an AE33, while AE51's performance ($R^2=0.76$) was poorer due to low sampling flow rate. STAP, was found to overestimate absorption coefficient at 880 nm by 10%, while AE51 and DWP overestimate it by 40% and 30%, respectively. However, with respect to eBC mass, the agreement was closer (within 7%). Taking advantage of the light weight AE51, on-flight intercomparison could be achieved for STAP and DWP. No correlation between the AE51 and STAP or DWP could be achieved for unconditioned high-time resolution (1 Hz) measurements. An improvement of the smoothing algorithm suggested by Hagler et al. (2011) was applied here leading to improved correlations ($R^2>0.70$) between miniature sensors (AE51, DWP and STAP). Based on four UAS flights, DWP and AE51 agreed very well (comparison slope equal to 0.92) with respect to the absorption coefficient at 880 nm ($b_{abs}(880)$), while STAP was found to underestimate $b_{abs}(880)$ by 12% which was consistent with the intercomparison performed at ground level against the AE33.

The Cyprus campaign took place at the Cyprus Atmospheric Observatory, a remote location distant by 7 km from the UAS runway and two of the miniature sensors (DWP and AE51) were evaluated on-flight against ground-based reference instruments, taking advantage of the elevation difference between the two sites. By comparison to the Athens campaign, the correlation of both sensors (against reference instruments) deteriorated because of low atmospheric aerosol concentrations (4 times lower) and reduced atmospheric variability (6 times lower). While DWP showed relatively good performance ($R^2=0.71$; N=91 data points), the poor performance of AE51 ($R^2=0.32$, N=91) was attributed to a lack of sensitivity of this sensor operating at a flow rate c.a. 10 times lower compared to DWP.

The overall potential use of miniature aerosol absorption sensor on-board UAS was illustrated with results of the campaign performed in Athens. During this campaign, the diurnal variability of the vertical distribution (0-1 km) of equivalent Black Carbon was investigated. It was found that eBC concentrations are not homogeneous in the boundary layer when it develops (PBL depth increases) and simultaneously absorbing material is emitted at ground level by traffic. Vertical homogeneity of eBC is reached in the afternoon, when the boundary layer height is stabilized and emissions at the ground are reduced.

Acknowledgements: The two field campaigns (Athens, Cyprus) are a contribution of the ACTRIS2 project that has received funding from the European Union's Horizon 2020 research and innovation program under grant agreement no. 654109. EU FP7

https://doi.org/10.5194/amt-2019-191
Preprint. Discussion started: 24 June 2019

Atmospheric Measurement Techniques Discussions

project BACCHUS (project number 603445) is acknowledged for financial support. MV acknowledges support from the DFG-Research Center/Cluster of Excellence "The Ocean in the Earth System-MARUM".

9. Nomenclature

Abbreviation	Description
ACTRIS	Aerosols, Clouds, and Trace Gases Research Infrastructure
ATN	Attenuation
b_{atn}	Attenuation coefficient
BACCHUS	Impact of Biogenic versus Anthropogenic emissions on Clouds and Climate; towards a Holistic UnderStanding
b_{abs}	Absorption coefficient
BC	Black carbon
BC_{bb}	BC related to biomass burning
C	Optical enhancement factor
CAO	Cyprus atmospheric observatory
DWP	Dual wavelength prototype
EARLINET	European Aerosol Research Lidar Network
eBC	Equivalent black carbon
EC	Elemental carbon
GUI	Graphical user interface
MAAP	Multiangle Absorption Photometer
MAC	Mass absorption coefficient
ONA	Optimized Noise-reduction Averaging
PBL	Planetary boundary layer
R	Filter loading parameter
STAP	Single channel Tri-color Absorption Photometer
UAS	Unmanned aerial systems
α	Angstrom exponent
λ	Wavelength
σ_{atn}	Mass attenuation cross section

10. References

Andreae, M. O. and Gelencsér, A.: Black carbon or brown carbon? The nature of light-absorbing carbonaceous aerosols, Atmos. Chem. Phys., 6, 3131-3148, https://doi.org/10.5194/acp-6-3131-2006, 2006.

Baars, H., Ansmann, A., Engelmann, R., Althausen, D., 2008. Continuous monitoring of the boundary-layer top with lidar. Atmos. Chem. Phys. 8, 7281–7296. https://doi.org/10.5194/acp-8-7281-2008

Bates, T.S., Quinn, P.K., Johnson, J.E., Corless, A., Brechtel, F.J., Stalin, S.E., Meinig, C., Burkhart, J.F., 2013. Measurements of atmospheric aerosol vertical distributions above Svalbard, Norway, using unmanned aerial systems (UAS). Atmos. Meas. Tech. 6, 2115–2120. https://doi.org/10.5194/amt-6-2115-2013

Birch, M.E., Cary, R.A., 1996. Elemental Carbon-Based Method for Monitoring Occupational Exposures to Particulate Diesel Exhaust. Aerosol Sci. Technol. 25, 221–241. https://doi.org/10.1080/02786829608965393

Bond, T.C., Anderson, T.L., Campbell, D., 1999. Calibration and Intercomparison of Filter-Based Measurements of Visible Light Absorption by Aerosols. Aerosol Sci. Technol. 30, 582–600. https://doi.org/10.1080/027868299304435

Bond T. C. and Bergstrom, R. W.: Light absorption by carbonaceous particles: an investigative review, *Aerosol Sci. Technol.*, 40, 27-67, DOI: 10.1080/02786820500421521, 2006.

Bond, T. C., Doherty, S. J,. Fahey, D. W., Forster, P. M., Berntsen, T., DeAngelo, B. J., Flanner, M. G., Ghan, S., Kärcher, B., Koch, D., Kinne, S., Kondo, Y., Quinn, P. K., Sarofim, M. C., Schultz, M. G., Schulz, M., Venkataraman, C., Zhang, H., Zhang, S., Bellouin, N., Guttikunda, S. K., Hopke, P. K., Jacobson, M. Z., Kaiser, J. W., Klimont, Z., Lohmann, U. J., Schwarz, P., Shindell, D., Storelvmo, T., Warren, S. G. and Zender C. S.: Bounding the role of black carbon in the climate system: A scientific assessment, *J. Geophys. Res. Atmos.*, 118, 5380–5552, doi:10.1002/jgrd.50171, 2013.

Collaud Coen, M., Weingartner, E., Apituley, A., Ceburnis, D., Fierz-Schmidhauser, R., Flentje, H., Henzing, J. S., Jennings, S. G., Moerman, M., Petzold, A., Schmid, O., and Baltensperger, U.: Minimizing light absorption measurement artifacts of the Aethalometer: evaluation of five correction algorithms, *Atmos. Meas. Tech.*, 3, 457–474, doi:10.5194/amt-3-457-2010, 2010.

Drinovec, L., Močnik, G., Zotter, P., Prévôt, A.S.H., Ruckstuhl, C., Coz, E., Rupakheti, M., Sciare, J., Müller, T., Wiedensohler, A., Hansen, A.D.A., 2015. The "dual-spot" Aethalometer: An improved measurement of aerosol black carbon with real-time loading compensation. Atmos. Meas. Tech. 8, 1965–1979. https://doi.org/10.5194/amt-8-1965-2015.

Engelmann, R., Kanitz, T., Baars, H., Heese, B., Althausen, D., Skupin, A., Wandinger, U., Komppula, M., Stachlewska, I. S., Amiridis, V., Marinou, E., Mattis, I., Linné, H., and Ansmann, A.: The automated multiwavelength Raman polarization and water-vapor lidar Polly^{XT}: the neXT generation, Atmos. Meas. Tech., 9, 1767-1784, https://doi.org/10.5194/amt-9-1767-2016, 2016.

Erel, Y., Dayan, U., Rabi, R., Rudich, Y., and Stein, M.: Tracing Trans-Boundary Transport of Pollutants by Mineral Dust, *Environ. Sci. Technol.*, 40, 2996–3005, 2006.

Atmospheric Measurement Techniques Discussions

Fernández, C. G., Picaud, S., Devel, M.: Calculations of the mass absorption cross sections for carbonaceous nanoparticles modeling soot, *J. Quant. Spectrosc. Radiat. Transfer*, 164, 69-81, http://dx.doi.org/10.1016/j.jqsrt.2015.05.011, 2015.

Ferrero, L., Mocnik, G., Ferrini, B. S., Perrone, M. G., Sangiorgi, G. and Bolzacchini, E.: Vertical profiles of aerosol absorption coefficient from micro-Aethalometer data and Mie calculation over Milan, *Sci Total Environ*, 409(14), 2824–2837, doi:10.1016/j.scitotenv.2011.04.022, 2011.

Florou, K., Papanastasiou, D.K., Pikridas, M., Kaltsonoudis, C., Louvaris, E., Gkatzelis, G.I., Patoulias, D., Mihalopoulos, N., Pandis, S.N., 2017. The contribution of wood burning and other pollution sources to wintertime organic aerosol levels in two Greek cities. Atmos. Chem. Phys. 17, 3145–3163. https://doi.org/10.5194/acp-17-3145-2017

Fourtziou, L., Liakakou, E., Stavroulas, I., Theodosi, C., Zarmpas, P., Psiloglou, B., Sciare, J., Maggos, T., Bairachtari, K., Bougiatioti, A., Gerasopoulos, E., Sarda-Estève, R., Bonnaire, N., Mihalopoulos, N., 2017. Multi-tracer approach to characterize domestic wood burning in Athens (Greece) during wintertime. Atmos. Environ. 148, 89–101. https://doi.org/https://doi.org/10.1016/j.atmosenv.2016.10.011

Gerasopoulos, E., Kouvarakis, G., Babasakalis, P., Vrekoussis, M., Putaud, J.-P., and Mihalopoulos, N: Origin and variability of particulate matter (PM_{10}) mass concentrations over the eastern Mediterranean, *Atmos. Environ.*, 40, 4679–4690, doi:10.1016/j.atmosenv.2006.04.020, 2006.

Hadley, O.L., Kirchstetter, T.W., 2012. Black-carbon reduction of snow albedo. Nat. Clim. Chang. 2, 437.

Hagler, G.S.W., Yelverton, T.L.B., Vedantham, R., Hansen, A.D.A., Turner, J.R., 2011. Post-processing method to reduce noise while preserving high time resolution in aethalometer real-time black carbon data. Aerosol Air Qual. Res. 11, 539–546. https://doi.org/10.4209/aaqr.2011.05.0055

Hale, G.M., Querry, M.R., 1972. Optical Constants of Water in the 200-nm to 200-μm Wavelength Region. Appl. Opt. 12, 555. https://doi.org/10.1364/ao.12.000555

Haywood, J., Boucher, O., 2000. Estimates of the direct and indirect radiative forcing due to tropospheric aerosols: A review. Rev. Geophys. 38, 513–543. https://doi.org/10.1029/1999RG000078

Hyvärinen, A.P., Vakkari, V., Laakso, L., Hooda, R.K., Sharma, V.P., Panwar, T.S., Beukes, J.P., Van Zyl, P.G., Josipovic, M., Garland, R.M., Andreae, M.O., Pöschl, U., Petzold, A., 2013. Correction for a measurement artifact of the Multi-Angle Absorption Photometer (MAAP) at high black carbon mass concentration levels. Atmos. Meas. Tech. 6, 81–90. https://doi.org/10.5194/amt-6-81-2013

Kalivitis, N., Gerasopoulos, E., Vrekoussis, M., Kouvarakis, G., Kubilay, N., Hatzianastassiou, N., Vardavas, I., and Mihalopoulos, M. Dust transport over the eastern Mediterranean derived from Total Ozone Mapping Spectrometer, Aerosol Robotic Network, and surface measurements, J. Geophys. Res., 112, D03202, doi:10.1029/2006JD007510

Kassianov, E., Berg, L.K., Pekour, M., Barnard, J., Chand, D., Comstock, J., Flynn, C., Sedlacek, A., Shilling, J., Telg, H., Tomlinson, J., Zelenyuk, A., Fast, J., 2018. A closure study of total scattering using airborne in situ measurements from the winter phase of TCAP. Atmosphere (Basel). 9. https://doi.org/10.3390/atmos9060228

Katich, J.M., Samset, B.H., Bui, T.P., Dollner, M., Froyd, K.D., Campuzano-Jost, P.,

https://doi.org/10.5194/amt-2019-191
Preprint. Discussion started: 24 June 2019

Atmospheric Measurement Techniques Discussions

Nault, B.A., Schroder, J.C., Weinzierl, B., Schwarz, J.P., 2018. Strong Contrast in Remote Black Carbon Aerosol Loadings Between the Atlantic and Pacific Basins. J. Geophys. Res. Atmos. 123, 13,386-13,395. https://doi.org/10.1029/2018JD029206

Kleanthous, S., Vrekoussis, M., Mihalopoulos, N., Kalabokas, P., Lelieveld, J., 2014. On the temporal and spatial variation of ozone in Cyprus. Sci. Total Environ. 476–477, 677–687. https://doi.org/10.1016/j.scitotenv.2013.12.101

Mamali, D., Marinou, E., Sciare, J., Pikridas, M., Kokkalis, P., Kottas, M., Binietoglou, I., Tsekeri, A., Keleshis, C., Engelmann, R., Baars, H., Ansmann, A., Amiridis, V., Russchenberg, H., Biskos, G., 2018. Vertical profiles of aerosol mass concentration derived by unmanned airborne in situ and remote sensing instruments during dust events. Atmos. Meas. Tech. 11, 2897–2910. https://doi.org/10.5194/amt-11-2897-2018

Marinou, E., Tesche, M., Nenes, A., Ansmann, A., Schrod, J., Mamali, D., Tsekeri, A., Pikridas, M., Baars, H., Engelmann, R., Voudouri, K.-A., Solomos, S., Sciare, J., Groβ, S., Amiridis, V., 2018. Retrieval of ice nucleating particle concentrations from lidar observations: Comparison with airborne in-situ measurements from UAVs. Atmos. Chem. Phys. Discuss. 1–37. https://doi.org/10.5194/acp-2018-1203

Myhre, G., Samset, B.H., Schulz, M., Balkanski, Y., Bauer, S., Berntsen, T.K., Bian, H., Bellouin, N., Chin, M., Diehl, T., Easter, R.C., Feichter, J., Ghan, S.J., Hauglustaine, D., Iversen, T., Kinne, S., Kirkevåg, A., Lamarque, J.F., Lin, G., Liu, X., Lund, M.T., Luo, G., Ma, X., Van Noije, T., Penner, J.E., Rasch, P.J., Ruiz, A., Seland, Skeie, R.B., Stier, P., Takemura, T., Tsigaridis, K., Wang, P., Wang, Z., Xu, L., Yu, H., Yu, F., Yoon, J.H., Zhang, K., Zhang, H., Zhou, C., 2013. Radiative forcing of the direct aerosol effect from AeroCom Phase II simulations. Atmos. Chem. Phys. 13, 1853–1877. https://doi.org/10.5194/acp-13-1853-2013

Petzold, A., Schönlinner, M., 2004. Multi-angle absorption photometry - A new method for the measurement of aerosol light absorption and atmospheric black carbon. J. Aerosol Sci. 35, 421–441. https://doi.org/10.1016/j.jaerosci.2003.09.005

Pikridas, M., Tasoglou, A., Florou, K., Pandis, S.N., 2013. Characterization of the origin of fine particulate matter in a medium size urban area in the Mediterranean. Atmos. Environ. 80, 264–274. https://doi.org/10.1016/j.atmosenv.2013.07.070

Pikridas, M., Vrekoussis, M., Sciare, J., Kleanthous, S., Vasiliadou, E., Kizas, C., Savvides, C., Mihalopoulos, N., 2018. Spatial and temporal (short and long-term) variability of submicron, fine and sub-10 μm particulate matter (PM1, PM2.5, PM10) in Cyprus. Atmos. Environ. 191, 79–93. https://doi.org/https://doi.org/10.1016/j.atmosenv.2018.07.048

Sandradewi, J., Prévôt, A.S.H., Szidat, S., Perron, N., Alfarra, M.R., Lanz, V.A., Weingartner, E., Baltensperger, U.R.S., 2008. Using aerosol light abosrption measurements for the quantitative determination of wood burning and traffic emission contribution to particulate matter. Environ. Sci. Technol. 42, 3316–3323. https://doi.org/10.1021/es702253m

Schrod, J., Weber, D., Drücke, J., Keleshis, C., Pikridas, M., Ebert, M., Cvetković, B., Nickovic, S., Marinou, E., Baars, H., Ansmann, A., Vrekoussis, M., Mihalopoulos, N., Sciare, J., Curtius, J., Bingemer, H.G., 2017. Ice nucleating particles over the Eastern Mediterranean measured by unmanned aircraft systems. Atmos. Chem. Phys. 17, 4817–4835. https://doi.org/10.5194/acp-17-4817-2017

Sedlacek, A.J., Buseck, P.R., Adachi, K., Onasch, T.B., Springston, S.R., Kleinman,

https://doi.org/10.5194/amt-2019-191
Preprint. Discussion started: 24 June 2019

Atmospheric Measurement Techniques Discussions

L., 2018. Formation and evolution of tar balls from northwestern US wildfires. Atmos. Chem. Phys. 18, 11289–11301. https://doi.org/10.5194/acp-18-11289-2018

Sheridan, P.J., Patrick Arnott, W., Ogren, J.A., Andrews, E., Atkinson, D.B., Covert, D.S., Moosmüller, H., Petzold, A., Schmid, B., Strawa, A.W., Varma, R., Virkkula, A., 2005. The reno aerosol optics study: An evaluation of aerosol absorption measurement methods. Aerosol Sci. Technol. 39, 1–16. https://doi.org/10.1080/027868290901891

Shiraiwa, M., Kondo, Y., Iwamoto, T. and Kita, K.: Amplification of light absorption of black carbon by organic coating, *Aerosol Sci. Technol.*, 44, 46-54, DOI: 10.1080/02786820903357686, 2010.

Slowik J. G., Cross, E. S., Han, J.-H., Davidotis, P., Onasch, T. B., Jayne, J. T., Williams, L. R., Canagaratna, M. R., Worsnop, D. R., Chakrabarty, R. K., Moosmüller, H., Arnott, W. P., Schwarz, J. P., Gao, R.-K., Fahey, D. W., Kok, G. L., Petzold, A.: An intercomparison of instruments measuring black carbon content of soot particles, *Aerosol Sci. Technol.*, 41, 295-314, DOI: 10.1080/02786820701197078, 2007.

Villa, T. F., Gonzalez, F., Miljievic, B., Ristovski, Z. D. and Morawska, L.: An overview of small unmanned aerial vehicles for air quality measurements: present applications and future prospectives, *Sensors*, 16, 1072, doi:10.3390/s16071072, 2016.

Virkkula, A., Ahlquist, N.C., Covert, D.S., Arnott, W.P., Sheridan, P.J., Quinn, P.K., Coffman, D.J.: Modification, calibration and a field test of an instrument for measuring light absorption by particles. *Aerosol Sci. Technol*. 39, 68-83, 2005.

Virkkula, A., Chi, X., Ding, A., Shen, Y., Nie, W., Qi, X., Zheng, L., Huang, X., Xie, Y., Wang, J., Petäjä, T. and Kulmala, M.: On the interpretation of the loading correction of the aethalometer, *Atmos. Meas. Tech.*,8, 4415-4427, doi:10.5194/amt-8-4415-2015, 2015.

Wang, R., Balkanski, Y., Boucher, O., Ciais, P., Schuster, G. L., Chevallier, F., Samset, B. H., Liu, J., Piao, S., Valari, M., Tao, S.: Estimation of global black carbon direct radiative forcing and its uncertainty constrained by observations, *J. Geophys. Res. Atmos.*, 121, 5948–5971, doi:10.1002/2015JD024326, 2016

Watson, J. G., Chow, J. C., and Chen, L.-W. A.: Summary of organic and elemental carbon/black carbon analysis methods and intercomparisons, *Aerosol Air Qual. Res.*, 5, 65–102, 2005.

Weingartner, E., Saathoff, H., Schnaiter, M., Streit, N., Bitnar, B. and Baltensperger, U.: Absorption of light by soot particles: determination of the absorption coefficient by means of aethalometers, *J. Aerosol Sci*., 34, 1445–1463, 2003

Wilcox, E.M., Thomas, R.M., Praveen, P.S., Pistone, K., Bender, F.A.-M., Ramanathan, V., 2016. Black carbon solar absorption suppresses turbulence in the atmospheric boundary layer. Proc. Natl. Acad. Sci. 113, 11794–11799. https://doi.org/10.1073/pnas.1525746113.

Zhang, H., Zhou, C., Wang, Z., Zhao, S., Jiangnan, L.: The influence of different black carbon and sulfate mixing methods on their optical and radiative properties, *J. Quant. Spectrosc. Radiat. Transfer*, 161, 105-116, http://dx.doi.org/10.1016/j.jqsrt.2015.04.002, 2015.

https://doi.org/10.5194/amt-2019-191
Preprint. Discussion started: 24 June 2019

Zíková, N., Vodička, P., Ludwig, W., Hitzenberger, R., Schwarz, J., 2016. On the use of the field Sunset semi-continuous analyzer to measure equivalent black carbon concentrations. Aerosol Sci. Technol. 50, 284–296. https://doi.org/10.1080/02786826.2016.1146819

https://doi.org/10.5194/amt-2019-191
Preprint. Discussion started: 24 June 2019

Atmospheric Measurement Techniques
Discussions

Table 1. Summary of UAS used during the Athens and Cyprus campaigns.

USRL Fleet of UAS	Type	MTOW	Payload*	Endurance*	Ceiling*
 Cruiser	Medium Size Fixed Wing	35 kg	12 kg	4 h	3k asl
 Skywalker X8	Small Size Fixed Wing	5 kg	3 kg	1 h	3 km asl
 DJi S1000+	Small Size Rotary Wing	11 kg	4 kg	30 min	1 km asl

* UAS characteristics as configured particularly for BACCHUS and ACTRIS campaigns

https://doi.org/10.5194/amt-2019-191
Preprint. Discussion started: 24 June 2019

Table 2. Summary of standardized properties of each attenuation monitor.

Manufacturer	Instrument name	Mass attenuation cross section (m^2 g^{-1})	Optical enhancement factor (C)	Reference
Magee Scientific	AE33	10730.48/λ	1.57	Drinovec et al., 2015
Magee Scientific	AE51	11000/λ	2.05	Ferrero et al., 2011
Brechtel	STAP	N/A*	N/A*	Ogren et al., 2010
Thermo Scientific	MAAP	6.6 at 670 nm	N/A	Petzold and Schönlinner, 2004
Custom made from AE51	Dual Wavelength Prototype (DWP)	11000/λ	2.05	N/A

* Equation 7 is used instead

https://doi.org/10.5194/amt-2019-191
Preprint. Discussion started: 24 June 2019

Table 3. Characteristics of the miniature absorption instruments.

Instrument Name	Flowrate (LPM)	Spot Area (m^2)	Wavelengths (nm)	Face Velocity ($m\ s^{-1}$)	Weight (g)	Time Response (s)
AE51	0.1-0.2	7.1×10^{-6}	880	0.5	280	1, 10, 30
DWP	2	7.1×10^{-6}	370, 880	4.7	1100	1
STAP	1.3	17.7×10^{-6}	445, 515,633	1.2	660	1

https://doi.org/10.5194/amt-2019-191
Preprint. Discussion started: 24 June 2019

Atmospheric Measurement Techniques Discussions

Table 4. Results from the comparison of the miniature sensors with ground based commercial instruments (AE33 and MAAP) shown in Fig. 5, 6 and 7

	eBC		$b_{abs}(370)\ Mm^{-1}$		$b_{abs}(880)\ Mm^{-1}$		*Angstrom Exponent*	
	slope ±95% CI	**Quality of fit (R^2)**	**slope ±95% CI**	**Quality of fit (R^2)**	**slope ±95% CI**	**Quality of fit (R^2)**	**slope ±95% CI**	**Quality of fit (R^2)**
				Athens campaign				
AE33	1.20±0.11	0.98	2.45±0.21	0.99	2.25±0.19	0.99	N/A	N/A
DWP	0.93±0.15	0.90	1.22±0.20	0.87	1.29±0.20	0.90	0.87±0.22	0.21
AE51	0.94±0.09	0.76	N/A	N/A	1.30±0.12	0.76	N/A	N/A
STAP	N/A	N/A	0.93±0.07	0.89	1.06±0.08	0.88	0.88±0.17	0.27
				Cyprus campaign				
AE33	1.13±0.05	0.89	1.93±0.09	0.88	1.83±0.08	0.89	N/A	N/A
DWP	0.94±0.20	0.71	0.83±0.18	0.68	1.20±0.26	0.71	0.44±0.28	0.1
AE51	1.22±0.52	0.32	N/A	N/A	1.55±0.66	0.32	N/A	N/A

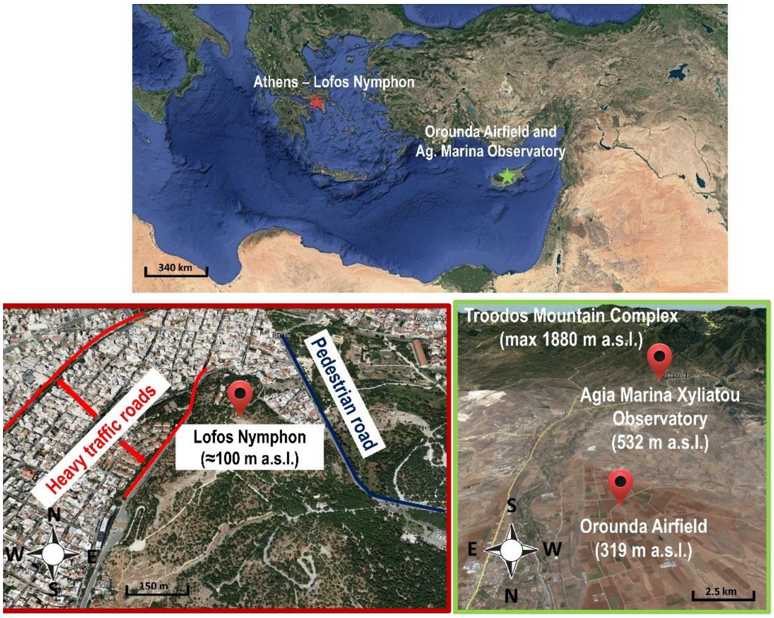

Figure 1. Upper panel: Location of the sampling sites in the Eastern Mediterranean (top) of the two sampling sites. During the Athens campaign sampling was conducted at Lofos Nymphon (bottom left) surrounded by busy traffic roads (red line) and a touristic area (blue line) free of motor vehicles. During the Cyprus campaign (bottom right) measurements using UAS was conducted at the Orounda airfield and ground based monitoring at the Agia Marina Xyliatoy Observatory at the foothills of the Troodos mountain complex. The elevation difference between these sites is noted.

https://doi.org/10.5194/amt-2019-191
Preprint. Discussion started: 24 June 2019

Figure 2: Aerial view of the Orounda runway in Cyprus.

https://doi.org/10.5194/amt-2019-191
Preprint. Discussion started: 24 June 2019

Atmospheric Measurement Techniques
Discussions
Open Access

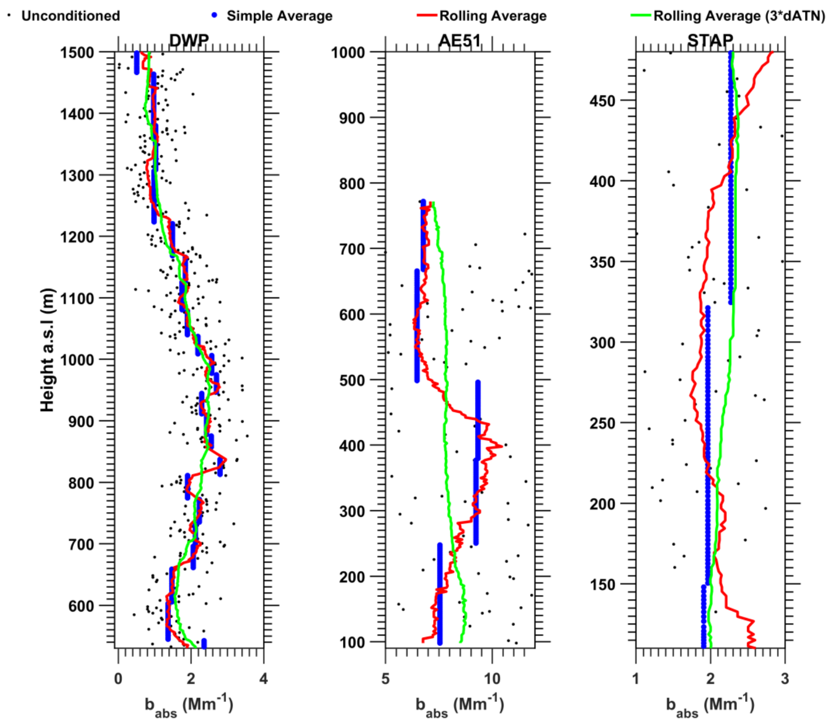

Figure 3. Examples of the use of the improved ONA algorithm for the three attenuation monitors examined in this study. Raw data (black dots) are shown against the traditional ONA algorithm (Hagler et al., 2011; blue dots), the improved ONA using a rolling average and the ΔATN proposed in Section 5 (red line), and the improved ONA using the rolling average but with increased ΔATN by a factor of 3 (oversmoothed- green line). The proposed ΔATN used are 0.01, 0.03, 0.03 for AE51, DWP and STAP, respectively.

https://doi.org/10.5194/amt-2019-191
Preprint. Discussion started: 24 June 2019

Atmospheric Measurement Techniques
Discussions

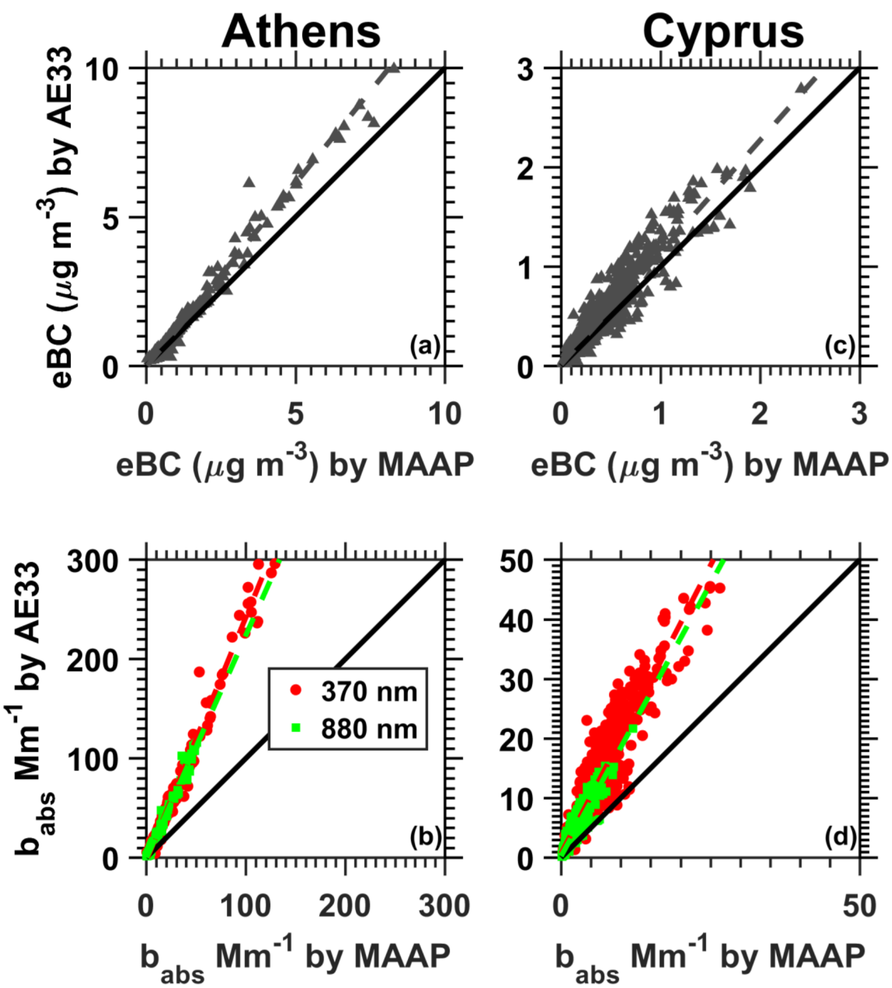

1219

1220 **Figure 4.** Comparison of AE33 against MAAP for eBC (a,c panels) and b_{abs} (b, d
1221 panels) at 370nm (red dots) and 880nm (green dots) during the Athens (a,c panels) and
1222 Cyprus (b,d panels) campaigns, respectively. Results are shown in Table 4.

https://doi.org/10.5194/amt-2019-191
Preprint. Discussion started: 24 June 2019

Atmospheric Measurement Techniques
Open Access
Discussions

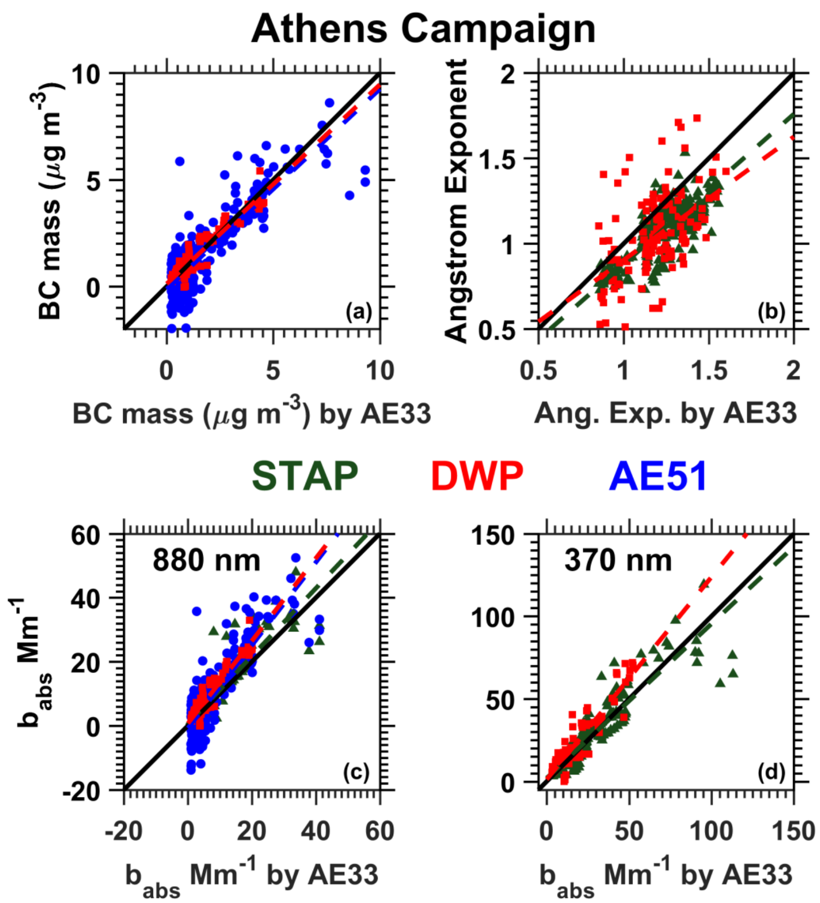

1223

1224 **Figure 5**. Comparison of miniature attenuation monitors whilst on the ground against
1225 the corrected AE33 during the Athens campaign with respect to eBC mass (a),
1226 absorption angstrom exponent (b), and the absorption coefficient at 880 nm (c) and 370
1227 nm (d). Results are shown in Table 4.

1228

https://doi.org/10.5194/amt-2019-191
Preprint. Discussion started: 24 June 2019

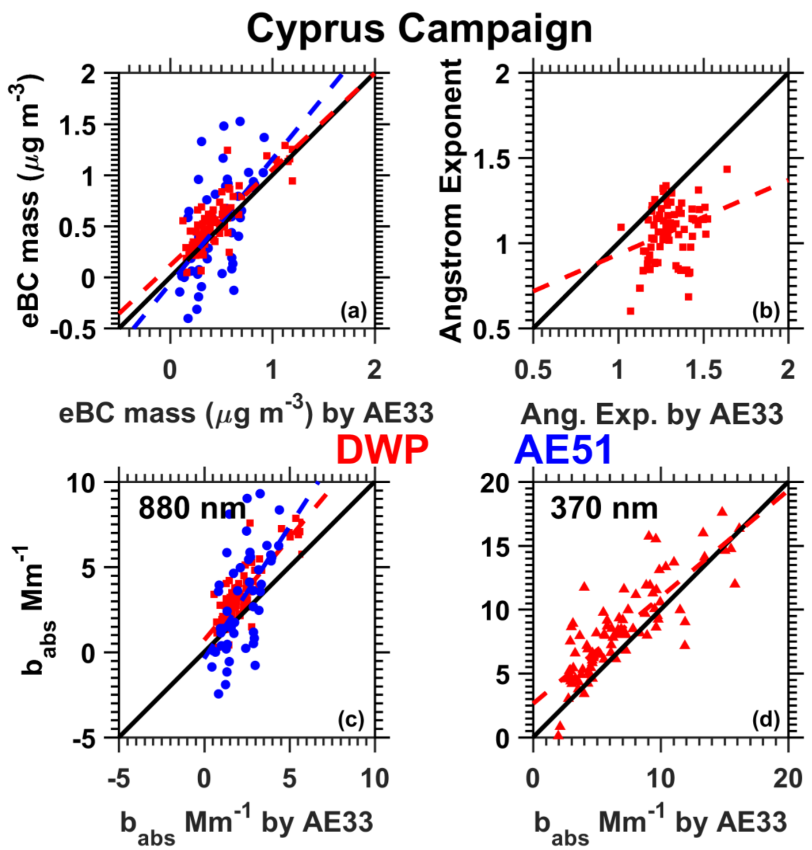

Figure 6. Comparison of miniature attenuation monitors while airborne against the corrected AE33 during the Cyprus campaign with respect to eBC mass (a), absorption angstrom exponent (b), and the absorption coefficient at 880 nm (c) and 370 nm (d). Miniature monitors sampled airborne. Results are shown in Table 4.

https://doi.org/10.5194/amt-2019-191
Preprint. Discussion started: 24 June 2019

Atmospheric Measurement Techniques
Discussions

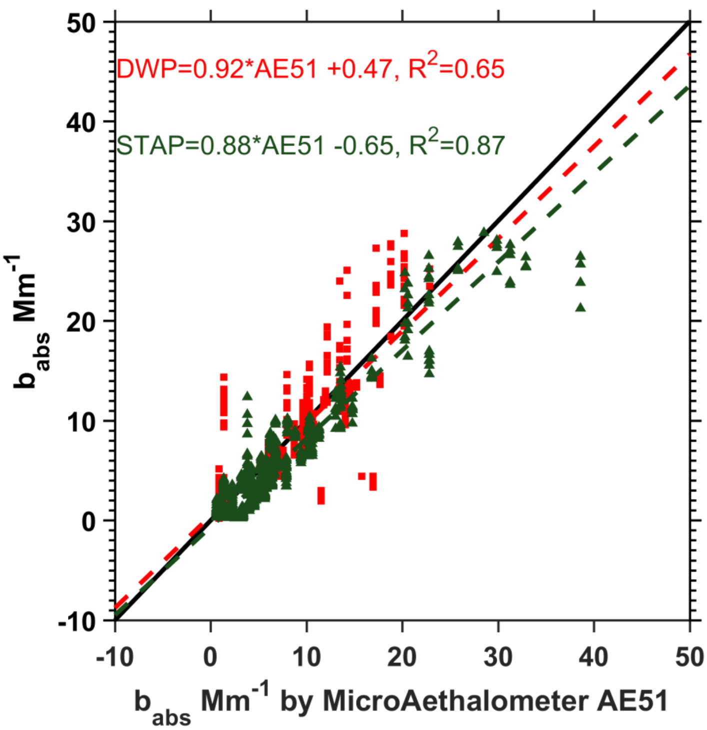

1240

1241 **Figure 7**. Comparison of AE51 against STAP (green triangles) and DWP (magenta
1242 squares) during eight flights of the Athens campaign. The reported agreement in the
1243 correlation suggests that no significant bias affected the monitors. The correlation
1244 deteriorates to (R^2=0.01) if data are not conditioned as suggested in Section 5.

1245

1246

1247

https://doi.org/10.5194/amt-2019-191
Preprint. Discussion started: 24 June 2019

Atmospheric Measurement Techniques
Discussions

1248 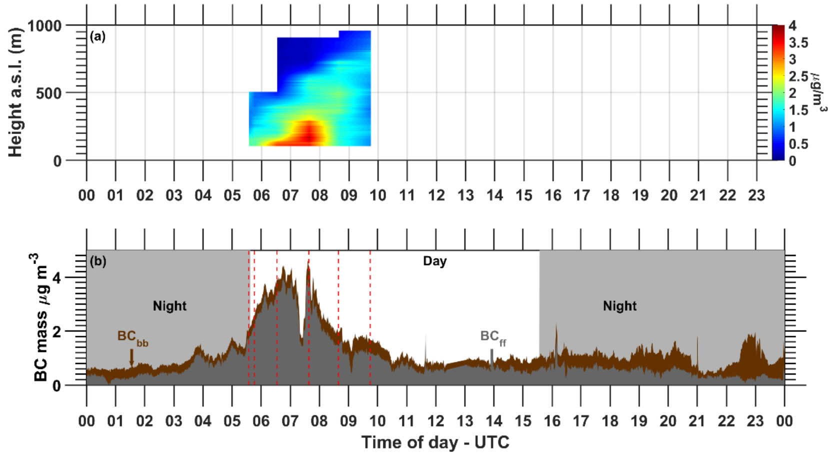

1249 **Figure 8**. Reconstruction of eBC mass vertical distribution (a) based on 6 flights
1250 between 19th January 2016 (Athens campaign) 05:30 and 09:30 (UTC). The actual
1251 vertical distributions are shown in Fig. 9. The corresponding ground measurements are
1252 also shown on panel (b). The concentration of BC from fossil fuel (ff) and biomass
1253 burning (bb) are shown with grey and brown colour, respectively. Dashed red lines
1254 indicate the start of each of the 6 flights the reconstructed eBC profiles was based upon.

1255

https://doi.org/10.5194/amt-2019-191
Preprint. Discussion started: 24 June 2019

Atmospheric Measurement Techniques
Open Access
EGU
Discussions

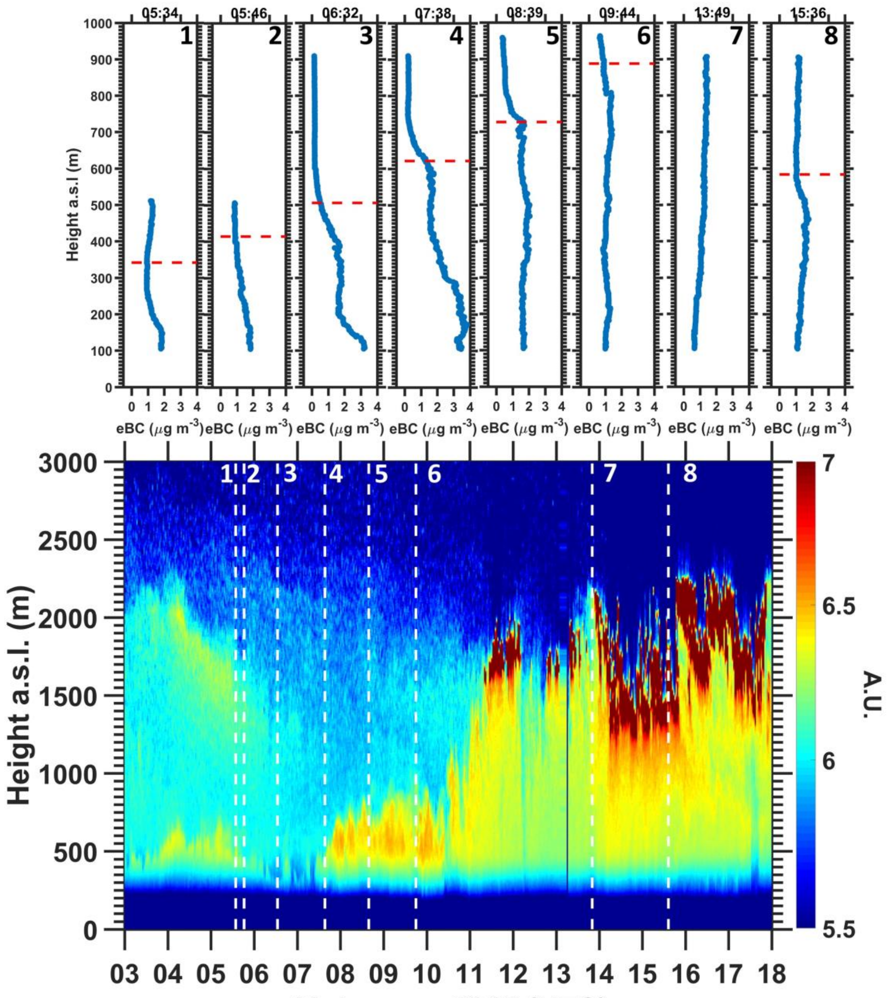

1256

1257 **Figure 9**. Vertical profiles (blue lines) of the eBC mass, measured during 19th January
1258 2016 (Athens campaign) accompanied by the mixing height (dashed red line) of the
1259 lower layer derived by Polly-XT measurements. During the 13:49 flight, mixing height
1260 was higher than the maximum altitude of flight and it is not shown. The corresponding
1261 time-height display of the 1064-nm range corrected signal measured with Polly-XT is
1262 also shown. Dashed white lines correspond to the start of each of the 8 flights performed
1263 during that day.

1264